Decomposition of Atmospheric Disturbances into Standing and Traveling Components, with Application to Northern Hemisphere Planetary Waves and Stratosphere–Troposphere Coupling

OLIVER WATT-MEYER AND PAUL J. KUSHNER

Department of Physics, University of Toronto, Toronto, Ontario, Canada

(Manuscript received 22 July 2014, in final form 26 September 2014)

ABSTRACT

This study updates a body of literature that aims to separate atmospheric disturbances into standing and traveling zonal wave components. Classical wavenumber–frequency analysis decomposes longitude- and time-dependent signals into contributions from distinct spatial and temporal scales. Here, an additional decomposition of the spectrum into standing and traveling components is described. Previous methods decompose the power spectrum into standing and traveling parts with no explicit allowance for covariance between the two. This study provides a simple method to calculate the variance of each of these components and the covariance between them. It is shown that this covariance is typically a significant portion of the variance of the total signal. The approach also preserves phase information and allows for the reconstruction of the real-space standing and traveling components.

The technique is applied to reanalysis wintertime geopotential height anomalies in the Northern Hemisphere in order to investigate planetary wave interference effects in stratosphere–troposphere coupling. The results show that for planetary waves 1–3, standing waves explain the largest portion of the variance at low frequencies. An exception is for wave 1 in the high-latitude troposphere, where there is a strong westward-traveling wave. Furthermore, the antinodes of the standing waves have preferred longitudes that tend to align with the extremes of the climatological wave, suggesting that standing waves contribute to a linear interference effect that has been shown to be an important part of stratosphere–troposphere interactions.

1. Introduction

Wavenumber–frequency spectral analysis is often used to decompose large-scale atmospheric flows into spatial and temporal Fourier harmonics (e.g., Hayashi 1971; Wheeler and Kiladis 1999), which can then be used to compute cross-spectra for quantities such as meridional heat or momentum flux (Randel and Held 1991). Here we consider the problem of further decomposing each Fourier harmonic into standing and traveling components. In this work a standing wave is defined to be like a standing wave on a string with fixed ends—that is, of the form $\cos(k\lambda)\cos(\omega t)$. It is the sum of two oppositely traveling waves of equal amplitude and phase speed: $2\cos(k\lambda)\cos(\omega t) = \cos(k\lambda - \omega t) + \cos(k\lambda + \omega t)$. Note that in some studies, ''standing wave'' is used to refer to the climatological zonal asymmetry; we will refer to this latter quantity simply as the climatological wave. Estimation of standing and traveling wave power spectra has been described previously (Hayashi 1973, 1977, 1979; Pratt 1976). However, the methods proposed by Hayashi and Pratt both suffer from the same issue: they exclusively decompose the power spectrum into standing and traveling parts with no possibility for any covariance between these wave structures. We will show that although such decompositions are not unique, typical prescriptions yield standing waves that are not orthogonal to the traveling waves and hence include significant covariance.

In this report, we propose a simple decomposition of the wavenumber–frequency spectrum into standing and traveling parts, calculate analytic expressions for the variance of each component and their covariance, and show how the decomposition can be used to reconstruct standing and traveling wave fields. While the techniques that we describe are quite general, we were motivated to carry out this analysis by particular issues related to

Corresponding author address: Oliver Watt-Meyer, Department of Physics, University of Toronto, 60 St. George St., Toronto ON M5S 1A7, Canada.
E-mail: oliverwm@atmosp.physics.utoronto.ca

DOI: 10.1175/JAS-D-14-0214.1

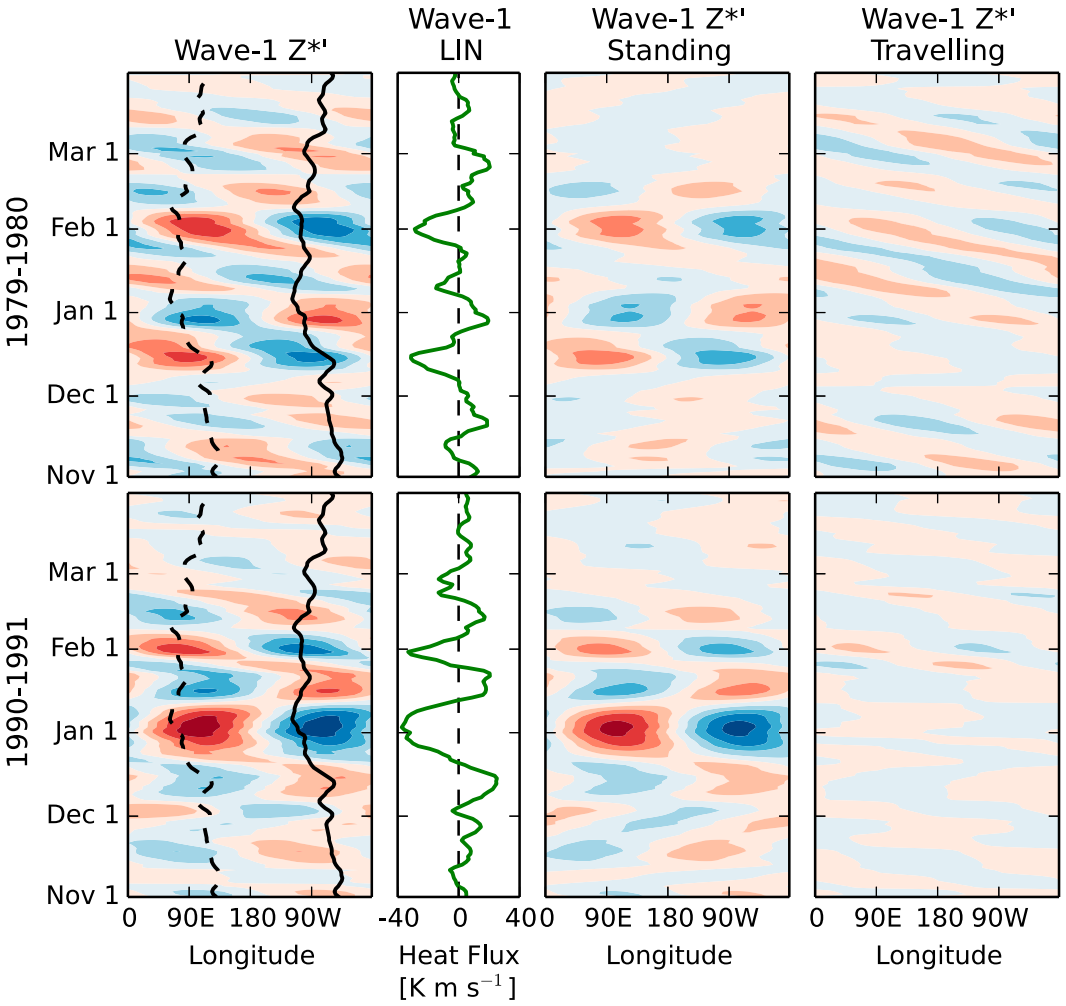

FIG. 1. Wave-1 $Z^{*\prime}$ and LIN heat flux at 60°N and 100 hPa for two NDJFM seasons: (top) 1979/80 and (bottom) 1990/91. (left)–(right) Wave-1 $Z^{*\prime}$, wave-1 component of LIN heat flux, wave-1 $Z^{*\prime}_{\mathrm{St}}$, and wave-1 $Z^{*\prime}_{\mathrm{Tr}}$. The contour levels for all the Hovmöller diagrams are ±(0, 100, 200, 300, 400, 500) m, where the reds are positive and blues are negative. The solid and dashed black lines on the farthest left panels show the daily position of the maximum and minimum of the wave 1 of Z^{*}_{c}. Note that for each row the two right panels sum to the leftmost panel.

wave-driven stratosphere–troposphere coupling in the Northern Hemisphere extratropics (Baldwin and Dunkerton 2001; Garfinkel et al. 2010; Shaw et al. 2010; Smith and Kushner 2012). Thus, we apply the technique to geopotential height anomalies in the Northern Hemisphere winter. Example case studies of interest are shown in Fig. 1. In the left column in Fig. 1 we show Hovmöller plots of the wave-1 geopotential height anomalies at 60°N and 100 hPa for the winter of 1979/80, which consisted of persistent westward-propagating wave-1 anomalies, and for the winter of 1990/91, which was dominated by a large-amplitude standing wave event. Our interest is in how these different wave anomalies interfere with the background climatology and, thus, drive fluctuations in the portion of the vertical flux of wave activity—as measured by the meridional eddy heat flux—that is linearly coherent with the background climatological wave (Nishii et al. 2009). We denote this quantity "LIN" (Smith and Kushner 2012). The second column in Fig. 1 shows the wave-1 component of LIN for each of these winter seasons. The positive and negative periods of LIN correspond to wave-1 anomalies being, respectively, in and out of phase with the wave-1 background climatology (the longitudes of the maximum and minimum of the daily wave-1 climatology are indicated by the solid and dashed black lines). A standing–traveling decomposition will allow us to determine whether fluctuations in LIN are being driven primarily by traveling waves of consistent amplitude propagating in and out of phase with the background or by standing waves fixed in space.

Computations of standing and traveling wave decompositions of the extratropical circulation have to

a large extent relied on the methods of Hayashi (1977, 1979) and Pratt (1976). These methods were summarized in the textbook by von Storch and Zwiers (1999). For example, Fraedrich and Böttger (1978) decompose the spectrum of geopotential heights at 500 hPa and 50°N into standing and traveling parts using a method that combines the techniques of Pratt and Hayashi. Their focus is on higher wavenumber and frequency disturbances, where the authors observe several distinct peaks in the spectrum. The authors suggest that differing types of baroclinic instability—associated with dry versus moist static stability—could be responsible for these separate peaks. Speth and Madden (1983), using the Hayashi (1977) method, highlight and investigate in more detail the presence of a high-latitude 15–30-day period westward-traveling wave-1 feature. Using the meridional and vertical structure of the feature's amplitude as evidence, the authors attribute it to a manifestation of the theoretically predicted 16-day wave (Haurwitz 1940; Madden 1979). Other studies have used Hayashi and Pratt's methods to determine whether the Madden–Julian oscillation is primarily a standing or propagating pattern (Zhang and Hendon 1997); to analyze the atmospheric variability in general circulation models and its dependence on the El Niño–Southern Oscillation (May 1999); and to quantify midlatitude tropospheric variability, and possible changes to it under global warming scenarios, in the Coupled Model Intercomparison Project phase 3 (Lucarini et al. 2007) and phase 5 (Di Biagio et al. 2014) ensembles.

These examples show the potentially wide applicability of standing–traveling wave decompositions. We will show that the previously used decomposition methods, however, do not explicitly account for the lack of uniqueness of these decompositions or for the nonorthogonality of the resulting wave fields. These shortcomings and their implications will be addressed in this report, which is structured as follows. Section 2 will outline the proposed standing–traveling decomposition, describe some simple analytical results, outline previously defined techniques, and describe the data to which we apply the analysis technique. Section 3 will show the results of applying the method to Northern Hemisphere geopotential height anomalies, including a detailed comparison with previous approaches and an overview of the climatological wavenumber–frequency spectra in the extratropics. To investigate planetary wave interference effects, we will compare the structure of the standing waves and the climatological wave field. Last, we will compute the vertical and time-lagged coherences of the standing and traveling waves at selected Northern Hemisphere extratropical locations using correlation-coherence analysis (Randel 1987). Section 4 will summarize the results and discuss implications for stratosphere–troposphere coupling.

2. Theory and data

a. Standing–traveling wave decomposition

This section describes our proposed decomposition of the wavenumber–frequency spectrum into standing and traveling parts. To begin, given some longitude- and time-dependent variable $q(\lambda, t)$, with daily frequency over a period of time of length T days and defined at N equally spaced points in longitude, the discrete 2D Fourier transform is computed as

$$\hat{q}_{k,j} = \sum_{n=0}^{N-1} \sum_{t=0}^{T-1} e^{-ik\lambda_n - i\omega_j t} q(\lambda_n, t), \tag{1}$$

where $\lambda_n = 2\pi n/N$ and $\omega_j = 2\pi j/T$, defined for $k = 0, \ldots, N-1$ (k is the planetary wavenumber) and $j = 0, \ldots, T-1$ (j is an integer index that corresponds to the frequency ω_j). For simplicity, $q(\lambda, t)$ is assumed to have zero zonal and time means, and N and T are assumed to be odd. Given that $q(\lambda, t)$ is real, as shown in the appendix, one can write the inverse transform as

$$q(\lambda, t) = \frac{2}{NT} \sum_{k=1}^{N_2} \sum_{j=1}^{T_2} q_{k,\pm j}(\lambda, t), \tag{2}$$

where $N_2 = (N-1)/2$, $T_2 = (T-1)/2$, and

$$q_{k,\pm j}(\lambda, t) = Q_{k,j} \cos(k\lambda + \omega_j t + \phi_{k,j}) + Q_{k,-j} \cos(k\lambda - \omega_j t + \phi_{k,-j}), \tag{3}$$

where we have used $\omega_{-j} = -\omega_j$ and where $Q_{k,j}$ and $\phi_{k,j}$ are the amplitude and phase of $\hat{q}_{k,j}$. That is, $\hat{q}_{k,j} = Q_{k,j} e^{i\phi_{k,j}}$, with $Q_{k,j}$ real and positive and $-\pi < \phi_{k,j} \le \pi$.

We now decompose the amplitudes $Q_{k,j}$ in Eq. (3) in order to express $q(\lambda, t)$ as a combination of standing and traveling waves at each wavenumber and frequency. Using the fact that a pure standing wave consists of two traveling waves of equal amplitude and phase speed moving in opposite directions, we define standing and traveling amplitudes as

$$Q^{\mathrm{St}}_{k,j} = \min(Q_{k,j}, Q_{k,-j}) \quad \text{and} \tag{4a}$$

$$Q^{\mathrm{Tr}}_{k,j} = Q_{k,j} - Q^{\mathrm{St}}_{k,j} \tag{4b}$$

and note that these definitions imply that $Q^{\mathrm{St}}_{k,j} = Q^{\mathrm{St}}_{k,-j}$ and that either $Q^{\mathrm{Tr}}_{k,j} = 0$ or $Q^{\mathrm{Tr}}_{k,-j} = 0$. Furthermore, we note that $Q^{\mathrm{St}}_{k,j}$ and $Q^{\mathrm{Tr}}_{k,j}$ are real and nonnegative. The

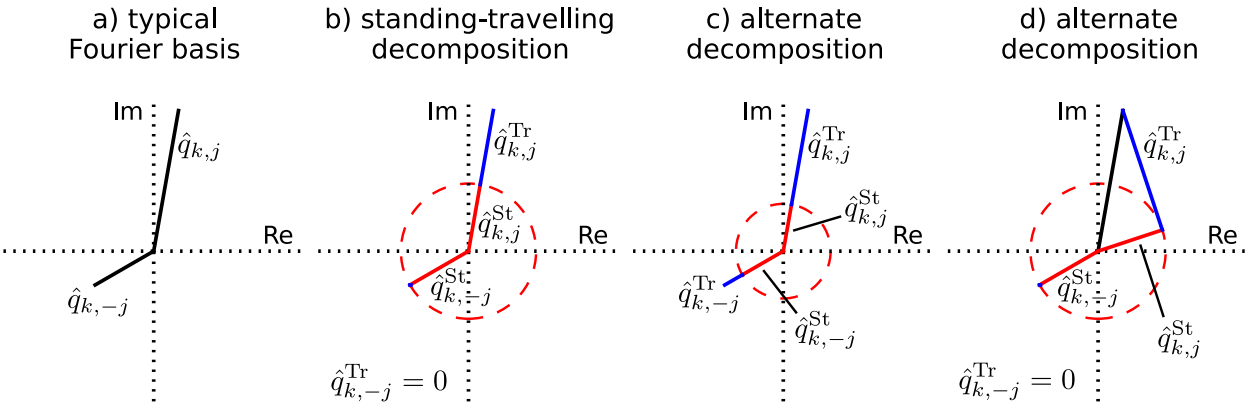

FIG. 2. Different possible decompositions of two Fourier coefficients into standing and traveling components. (a) Two arbitrary Fourier coefficients [see Eq. (1)] corresponding to the same wavenumber and opposite frequencies, plotted on the complex plane. (b) Decomposition of these two coefficients into standing (red) and traveling (blue) parts as implemented in this paper, following Eq. (4). (c) An alternate decomposition in which there are traveling waves propagating in both directions. (d) An alternate decomposition in which the phases of the standing and traveling components are allowed to differ from the phase of the total Fourier coefficient. In all cases, the standing wave amplitude is equal for $+j$ and $-j$.

phases of the standing and traveling components are set to be equal to the original Fourier coefficient phases; that is, $\phi^{\mathrm{St}}_{k,j} = \phi^{\mathrm{Tr}}_{k,j} = \phi_{k,j}$. A phasor representation in the complex plane of this decomposition of two Fourier coefficients $\hat{q}_{k,\pm j}$ into standing and traveling components is given in Figs. 2a and 2b. Alternative decompositions shown in Figs. 2c and 2d will be described in section 2b. Note that although we define the standing waves amplitude for both positive and negative frequencies, since our definition ensures the standing wave power is symmetric with respect to frequency, we could equivalently consider a "one sided" spectrum for the standing wave, as in some previous works (e.g., Fraedrich and Böttger 1978).

One of the main uses of the Fourier transform is to decompose the total variance of a signal into contributions from different wavenumbers and frequencies. From Parseval's theorem, written here using the same assumptions on $q(\lambda, t)$ as above, we have

$$\sum_{n=0}^{N-1}\sum_{t=0}^{T-1}[q(\lambda_n,t)]^2 = \frac{2}{NT}\sum_{k=1}^{N_2}\sum_{j=-T_2}^{T_2}(Q_{k,j})^2. \quad (5)$$

Furthermore, from Eq. (4b), we have

$$(Q_{k,j})^2 = (Q^{\mathrm{St}}_{k,j})^2 + (Q^{\mathrm{Tr}}_{k,j})^2 + 2Q^{\mathrm{St}}_{k,j}Q^{\mathrm{Tr}}_{k,j}. \quad (6)$$

Thus, the variance of the signal $q(\lambda, t)$ is decomposed at each wavenumber and frequency into a standing part, a traveling part, and a term that represents the covariance between the two parts. Note that since $Q^{\mathrm{St}}_{k,j}$ and $Q^{\mathrm{Tr}}_{k,j}$ are greater than or equal to zero, the covariance term is always nonnegative. This is to be expected: since in the definition of the standing and traveling parts of the signal we maintain the same phases $\phi_{k,j}$, the traveling wave will always positively correlate with one of the components of the standing wave.

In our decomposition the standing waves have an easily defined structure. At each wavenumber and pair of frequencies, the standing wave can be written as

$$\begin{aligned} q^{\mathrm{St}}_{k,\pm j}(\lambda,t) &= \frac{2}{NT}Q^{\mathrm{St}}_{k,j}\cos(k\lambda + \omega_j t + \phi_{k,j}) \\ &\quad + \frac{2}{NT}Q^{\mathrm{St}}_{k,-j}\cos(k\lambda - \omega_j t + \phi_{k,-j}) \\ &= \frac{4}{NT}Q^{\mathrm{St}}_{k,j}\cos(k\lambda + \overline{\phi}_{k,j})\cos(\omega_j t + \Delta\phi_{k,j}), \end{aligned} \quad (7)$$

where

$$\overline{\phi}_{k,j} = \frac{1}{2}(\phi_{k,j} + \phi_{k,-j}), \quad \Delta\phi_{k,j} = \frac{1}{2}(\phi_{k,j} - \phi_{k,-j}). \quad (8)$$

Thus, the standing wave corresponding to the wavenumber–frequency pair $(k, \omega_{\pm j})$ will have its crests and troughs at longitudes of $\lambda = (1/k)(\pi m - \overline{\phi}_{k,j})$, where m is an integer. It is shown in the appendix that $\overline{\phi}_{k,j}$ gives the same result for the positions of the antinodes as the formula given by Hayashi [e.g., Eq. (4.5) in Hayashi (1977)].

We are also interested in examining the typical behavior of standing and traveling waves consisting of more than one frequency across one or more seasons. To this end, we compute the variance over time of $q_k(\lambda, t) = (2/NT)\sum_{j=1}^{T_2} q_{k,\pm j}(\lambda, t)$. As demonstrated in the appendix, using the orthogonality of the cosine basis functions, one can show that

$$\mathrm{var}(q_k)(\lambda) = \frac{1}{T}\sum_{t=0}^{T-1}[q_k(\lambda,t)]^2$$
$$= \frac{2}{N^2T^2}\sum_{j=-T_2}^{T_2}[Q_{k,j}^2 + 2Q_{k,j}Q_{k,-j}\cos^2(k\lambda + \overline{\phi}_{k,j}) - Q_{k,j}Q_{k,-j}], \quad (9)$$

where $\overline{\phi}_{k,j}$ was defined in Eq. (8). If the signal $q_k(\lambda, t)$ is the sum of pure standing waves (i.e., $Q_{k,j} = Q_{k,-j}$) then Eq. (9) simplifies to

$$\mathrm{var}(q_k^{\mathrm{St}})(\lambda) = \frac{4}{N^2T^2}\sum_{j=-T_2}^{T_2} Q_{k,j}^2\cos^2(k\lambda + \overline{\phi}_{k,j}). \quad (10)$$

On the other hand, if our signal is the sum of pure traveling waves (i.e., either $Q_{k,j} = 0$ or $Q_{k,-j} = 0$ for every j; i.e., $Q_{k,j}Q_{k,-j} = 0$), then Eq. (9) simplifies to

$$\mathrm{var}(q_k^{\mathrm{Tr}})(\lambda) = \frac{2}{N^2T^2}\sum_{j=-T_2}^{T_2} Q_{k,j}^2. \quad (11)$$

b. *Alternate decompositions*

Because the standing and traveling waves at the same wavenumber and frequency are not orthogonal, the decomposition defined in Eq. (4) is not unique. For example, one could assign less amplitude to the standing wave and have traveling waves moving in both directions at each absolute frequency, as in Hayashi (1977). An example of this is shown in Fig. 2c. Furthermore, if one allows for the phases of the standing and traveling components to be different, then this allows another set of possibilities for the decomposition, an example of which is shown in Fig. 2d. Nevertheless, we argue that our choice defined in Eq. (4) is a natural decomposition to work with for a number of reasons. First, we reject the possibility of having traveling waves moving in both directions at the same wavenumber and phase speed, as in Fig. 2c, since these will just add up to an additional standing wave at this frequency. Second, we choose to keep the same phases for the standing and traveling components, because this is the simplest choice and because it ensures that the standing and traveling parts of the signal each have the maximum correlation with the total signal.

Note that if we allow the phases of the standing and traveling components to vary, as in Fig. 2d, the covariance can also be negative or zero. In particular, assuming only that $\hat{q}_{k,j} = \hat{q}_{k,j}^{\mathrm{St}} + \hat{q}_{k,j}^{\mathrm{Tr}}$, we can generalize Eq. (6) to

$$(Q_{k,j})^2 = (Q_{k,j}^{\mathrm{St}})^2 + (Q_{k,j}^{\mathrm{Tr}})^2 + 2Q_{k,j}^{\mathrm{St}}Q_{k,j}^{\mathrm{Tr}}\cos(\phi_{k,j}^{\mathrm{St}} - \phi_{k,j}^{\mathrm{Tr}}). \quad (12)$$

When $\phi_{k,j}^{\mathrm{St}} = \phi_{k,j}^{\mathrm{Tr}}$ as before, we recover Eq. (6) and the covariance is strictly positive. However, it is also possible to force $\phi_{k,j}^{\mathrm{St}} - \phi_{k,j}^{\mathrm{Tr}} = \pm\pi/2$ (one of these cases is illustrated in Fig. 2d) in which case the covariance will be zero. Nevertheless, the $\phi_{k,j}^{\mathrm{St}} = \phi_{k,j}^{\mathrm{Tr}}$ case is the most intuitive decomposition because it maximizes the correlation between each of the standing and traveling components and the total signal. This follows from the fact that the Fourier coefficients for the standing and traveling waves are parallel to the total coefficient in the complex plane (as in Fig. 2b).

As far as we are aware, all standing–traveling decompositions discussed in the literature (Hayashi 1973, 1977, 1979; Pratt 1976) do not explicitly account for the covariance term between standing and traveling waves. The authors generally take it as an assumption that the standing and traveling waves will be independent, although they do recognize that this is not always actually the case. In particular, they require that, written in our notation, either $(Q_{k,j})^2 = (Q_{k,j}^{\mathrm{St}})^2 + (Q_{k,j}^{\mathrm{Tr}})^2 + \text{noise}$ (Pratt 1976) or $(Q_{k,j})^2 = (Q_{k,j}^{\mathrm{St}})^2 + (Q_{k,j}^{\mathrm{Tr}})^2$ (Hayashi 1977) without any explicit representation of covariance between the standing and traveling parts of the signal.

We thus identify two distinct advances arising from our technique. First, we can precisely account for and calculate the often significant contribution from the joint variability of standing and traveling waves. Second, it is also straightforward to reconstruct the real-space standing and traveling parts of the signal,[1] which is something that is not simple to do with the other techniques.

c. *Other techniques*

Some previous techniques for computing the wavenumber–frequency spectrum, starting with Hayashi (1971), take a somewhat different approach than what we have described above. They begin by computing a spatial Fourier transform of $q(\lambda, t)$ at each time step and defining $c_k(t)$ and $s_k(t)$ as the time series for the cosine and sine coefficients at wavenumber k (again, we are assuming the zonal mean of q is zero):

$$q(\lambda,t) = \sum_{k=1}^{N}[c_k(t)\cos(k\lambda) + s_k(t)\sin(k\lambda)]. \quad (13)$$

[1] To do this, simply use the inverse transform given in Eqs. (2) and (3) with the standing or traveling amplitudes, $Q_{k,j}^{\mathrm{St}}$ or $Q_{k,j}^{\mathrm{Tr}}$, instead of the total amplitude $Q_{k,j}$.

The wavenumber–frequency spectrum is then defined as [see also von Storch and Zwiers (1999)]

$$P_{k,\omega}(q) = \frac{P_\omega(c_k) + P_\omega(s_k)}{2} + Q_\omega(c_k, s_k), \qquad (14)$$

where $P_\omega(c_k)$ and $P_\omega(s_k)$ are the power spectra of $c_k(t)$ and $s_k(t)$, respectively, and $Q_\omega(c_k, s_k)$ is the quadrature spectrum (i.e., imaginary part of the cross-spectrum) between the two. Note that, as shown by Tsay (1974), $P_{k,\omega}(q)$ is equal to the 2D Fourier amplitudes squared $|\hat{q}_{k,\omega_j}|^2$ where $\hat{q}_{k,\omega_j}$ was defined in Eq. (1).

Pratt (1976) and Hayashi (1977) define the standing wave variance as

$$P^{\mathrm{St}}_{k,\omega}(q) = \sqrt{\frac{1}{4}[P_\omega(c_k) - P_\omega(s_k)]^2 + K^2_\omega(c_k, s_k)}, \qquad (15)$$

where $K_\omega(c_k, s_k)$ is the cospectrum between $c_k(t)$ and $s_k(t)$.

Pratt and Hayashi differ in how they define the propagating part of the variance. Pratt defines the traveling variance as the difference between the eastward and westward components, or,

$$P^{\mathrm{Tr}}_{k,\omega}(q) = 2|Q_\omega(c_k, s_k)|. \qquad (16)$$

The direction of propagation is defined by whether $P_{k,\omega}$ or $P_{k,-\omega}$ is greater. By Pratt's definition, there is no guarantee that the standing and propagating components of the variance add up to the total wavenumber–frequency spectrum. Hayashi, on the other hand, simply defines the propagating variance as the total wavenumber–frequency spectrum minus the standing portion [e.g., Eq. (5.9) in Hayashi (1977)]. However, this can lead to negative powers for the propagating variance, since the standing wave variance as defined in Eq. (15) can sometimes be larger than the total wavenumber–frequency spectrum. Hayashi states this is most often an issue when there is insufficient smoothing in the frequency domain. There are two main differences between our technique and those of Pratt and Hayashi. First, we make no assumption about the independence of the traveling and standing waves, unlike the previous authors [e.g., see section 5 of Hayashi (1977)]. Second, our decomposition is based on the 2D Fourier coefficients themselves, as opposed to the power, co-, and quadrature spectra as in Eqs. (15) and (16).

We point out that there is some confusion in the literature about the Pratt and Hayashi techniques. Von Storch and Zwiers (1999) correctly describe how Pratt defines the traveling wave variance [Eq. (16)] but incorrectly state that Pratt defines the standing variance as the remainder of the total. This is actually how Fraedrich and Böttger (1978) explain the standing–traveling decomposition, effectively mixing the Pratt and Hayashi techniques. In section 3a, we will show results for the standing–traveling decomposition as we define it, compared to the two methods described in von Storch and Zwiers (1999).

d. Data and notation

We apply the analysis technique to 1979–2013 daily-mean geopotential height from the Interim European Centre for Medium-Range Weather Forecasts (ECMWF) Re-Analysis (ERA-Interim) (Dee et al. 2011). The data are on a 1.5° × 1.5° latitude–longitude grid, on 37 vertical levels ranging from 1000 to 1 hPa. We first remove the zonal mean and the daily climatology, which is computed by averaging each calendar day over all 35 years of the dataset. We use a superscript asterisk to denote the deviation from the zonal mean and a prime to denote the climatological anomaly:

$$Z^* = Z - \{Z\}, \quad Z' = Z - Z_c, \qquad (17)$$

where $\{Z\}$ and Z_c are the zonal and daily climatological means of Z, respectively.

The spectral analysis is then applied to $Z^{*\prime}$ separately at each latitude and pressure level, on 151-day periods starting 1 November of each year (thus, on non–leap years, the period is from 1 November to 31 March, and on leap years it is until 30 March). Note that before applying the spectral analysis, we linearly detrend and remove the time mean from the data over each winter period, as in Wheeler and Kiladis (1999). This does not have a major impact on our results since we have already removed the climatology. Although we compute the spectral decompositions independently at each latitude and pressure, in section 3f we will use the statistical method of Randel (1987) to examine aspects of the wave structures' spatial and temporally lagged coherence.

Following Randel and Held (1991), we use a normalized Gaussian spectral window of the form

$$W(\omega_j - \omega_{j_0}) \propto e^{-[(j-j_0)/\Delta j]^2} \qquad (18)$$

to smooth the power spectra about the frequency ω_{j_0}. Here, $W(\omega_j - \omega_{j_0})$ is the weight given to the spectrum at frequency ω_j for computing the smoothed power at ω_{j_0}. The Δj term is the width of the Gaussian window in terms of the frequency index, which we take to be $\Delta j = 1.5$. We are able to have a higher spectral resolution (smaller Δj) than Randel and Held (1991) because we are averaging our spectra over 34 winter seasons, as opposed to only 7.

Note that we apply the smoothing directly to each of the three terms on the right-hand side of Eq. (6) after having made the standing–traveling decomposition. This is in contrast to Hayashi and Pratt, who compute

smoothed spectra before making the standing and traveling decomposition (Pratt 1976). For comparison, we will also show some results in section 3a, where we smooth the wavenumber–frequency spectrum before making the decomposition into standing and traveling parts. For our method, this is slightly more involved because our decomposition is actually based on the amplitudes, not the amplitudes squared. Thus, to make the cleanest possible comparison with Hayashi and Pratt in section 3a, we square the amplitudes, then smooth, and then take the square root to get smoothed amplitudes, upon which we apply the decomposition into standing and traveling components following Eq. (4). Finally, we point out that we only smooth the spectra for display (e.g., in Fig. 4) but not when reconstructing the standing and traveling signals $q^{\mathrm{St}}(\lambda, t)$ and $q^{\mathrm{Tr}}(\lambda, t)$.

3. Results

a. Methods comparison

We begin by showing the various steps taken to compute the final, smoothed, wavenumber–frequency spectra, including the decomposition into standing and traveling waves. We show all the steps for the wave-1 component of $Z^{*\prime}$ for the 1979/80 year, which was shown in Fig. 1. For comparison, we will also show the standing–traveling decomposition as computed by following the methods of Hayashi and Pratt and by a version of our method that is more consistent with the Hayashi and Pratt methods.

Figure 3a shows the normalized[2] wave-1 component of the raw wavenumber–frequency spectrum [i.e., $(2/N^2T)(Z_{k,j})^2$]. Since we are showing results specific for geopotential heights, we write $Z_{k,j}$ here instead of $Q_{k,j}$ as in section 2. The zero-frequency component is plotted at the center of the figure, with westward-moving waves [positive ω_j in Eq. (2)] on the left side and eastward-moving waves (negative ω_j) on the right side. The absolute value of frequency increases moving away from the center of the figure, and we omit the frequencies higher than $0.1\,\mathrm{day}^{-1}$ since they contain negligible power for this year, latitude, and pressure level. Note that the zero-frequency component has zero amplitude because we have removed the time mean before computing the spectrum. Furthermore, the westward power is generally higher than the eastward power, indicative of a prominent westward-traveling wave.

Next, the decomposition into standing and traveling components is made based on the Fourier amplitudes

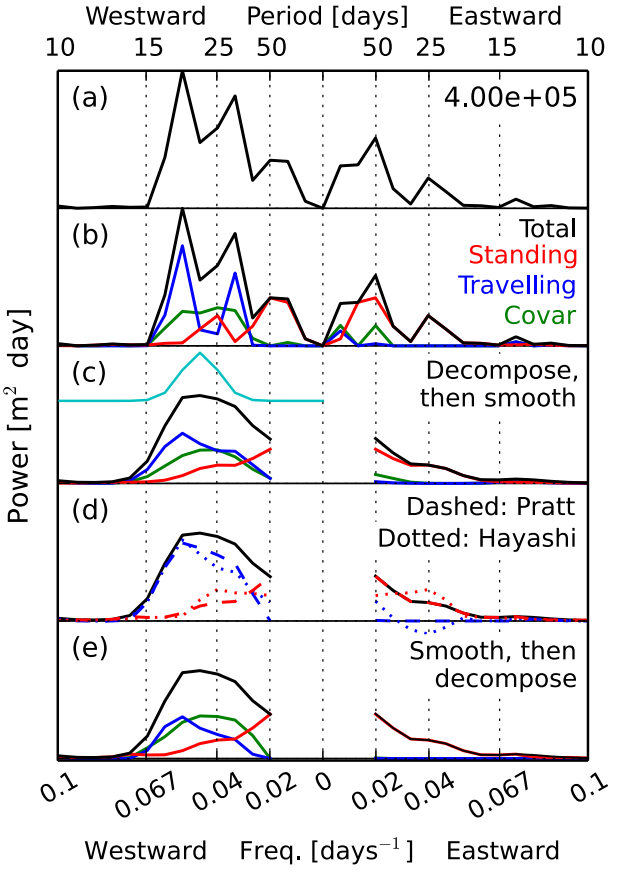

FIG. 3. Different versions of the wave-1 component of the wavenumber–frequency spectrum of NDJFM 1979/80 $Z^{*\prime}$ at 60°N and 100 hPa. (a) Unsmoothed wavenumber–frequency spectrum normalized such that integrating over frequency will give the wave-1 variance [i.e., we plot $(2/N^2T)Z_{k,j}^2$]. The number in the top-right corner gives the maximum value achieved by the spectrum over all frequencies (m^2 day). (b) Decomposition of the unsmoothed spectrum into standing (red), traveling (blue), and covariance (green) terms according to Eq. (6). (c) Spectra from (b) smoothed with a Gaussian window, which is shown by the thin cyan line [see Eq. (18); width is $\Delta j = 1.5$]. (d) Decompositions of the smoothed wavenumber–frequency spectrum into standing (red) and traveling (blue) components according to Pratt (1976) (dashed) and Hayashi (1977) (dotted). (e) Decomposition of the smoothed wavenumber–frequency spectrum into standing, traveling, and covariance components using our method [as opposed to (c), here the smoothing is performed before the standing–traveling decomposition; see discussion in section 2d]. For the smoothed spectra, we only plot the well-resolved frequencies. Note that all spectra are plotted on the same scale as indicated in (a).

(which are not shown) using Eq. (4). In Fig. 3b, we replot the total amplitudes squared and also show the three terms in Eq. (6): the standing variance $(Z_{k,j}^{\mathrm{St}})^2$ in red, the traveling variance $(Z_{k,j}^{\mathrm{Tr}})^2$ in blue, and the covariance between the two $2Z_{k,j}^{\mathrm{St}}Z_{k,j}^{\mathrm{Tr}}$ in green (the same normalization as in Fig. 3a is used in all cases). There is substantial westward-traveling wave variance between periods of

[2] The normalization is chosen such that summing the spectrum over positive wavenumbers and integrating over all frequencies will recover the total time–longitude variance of the original signal.

15–30 days, while standing waves dominate at the lowest frequencies. We also have the expected properties that $Z^{St}_{k,j} = Z^{St}_{k,-j}$ and that either $Z^{Tr}_{k,j} = 0$ or $Z^{Tr}_{k,-j} = 0$. Next, we smooth each of the terms individually, as discussed in section 2d. The smoothed spectra, as well as the Gaussian window used to do the smoothing, are plotted in Fig. 3c.

We also compare with the methods described by von Storch and Zwiers (1999), which are based on those in Pratt (1976) and Hayashi (1977). However, as noted in section 2c, the Pratt method described in von Storch and Zwiers (1999) is actually a conflation of the true Pratt and Hayashi methods. For the remainder of the paper, when we discuss the ''Pratt'' method, we refer to the method attributed to Pratt that is described in section 11.5.7 of von Storch and Zwiers (1999).

In Fig. 3d, the decompositions described by Pratt and Hayashi are shown. The variance is exclusively decomposed into standing and traveling portions, without any covariance. Furthermore, note that these authors suggest computing a smoothed wavenumber–frequency spectrum before making the decomposition into standing and traveling components. This is what has been done in Fig. 3d, and so for comparison, in Fig. 3e we show the results for our decomposition based on the presmoothed total spectrum (see discussion in section 2d). Our method gives identical results for the standing wave power as the Pratt method when consistent smoothing is done, and the Hayashi standing wave power is generally similar. However, both Pratt and Hayashi attribute the remaining variance exclusively to the traveling wave, whereas we assign it to both the traveling wave and the covariance between the standing and traveling waves. This leads to a major reduction in the variance attributed exclusively to the traveling wave in our method. Also, note that Hayashi's method gives a negative traveling wave power at some frequencies—a clearly nonphysical result.

b. *Reconstruction of standing and traveling wave fields*

Using Eqs. (2) and (3) with the decomposed amplitudes $Q^{St}_{k,j}$ and $Q^{Tr}_{k,j}$ replacing the total amplitudes $Q_{k,j}$, one can reconstruct the standing and traveling parts of the signal $q(\lambda, t)$. To accurately reconstruct the original signal, it is necessary to use the unsmoothed amplitudes. In the two right columns of Fig. 1, the wave-1 portions of the standing and traveling signals are plotted for 60°N and 100 hPa for the 1979/80 and 1990/91 winters. As we had expected from viewing the total wave-1 anomaly, the 1979/80 year contains a consistent westward-propagating wave. However, the quantitative decomposition that we make allows us to also recognize the significant contribution of standing waves to the variability this year. For the 1990/91 year, we see the expected result: the standing wave field looks very similar to the total field, while the traveling wave field generally has small amplitudes. Note that the standing and traveling wave reconstructions are not ''pure'' standing or traveling waves because they are the combination of a range of frequencies. As well, since the method naturally focuses on explaining the largest-variance features, in some cases it is possible for the technique to generate somewhat spurious results in the low-amplitude part of the signal. For example, in Fig. 1, the standing part of the signal for mid-November–December 1990 contains an eastward-propagating feature. Nevertheless, it is of much smaller amplitude than the standing wave feature later in the season, which is accurately captured.

c. *Climatological spectra at 60°N*

The frequency spectra at 60°N for three different vertical levels and for planetary waves 1–3 are shown in Fig. 4. Note that in Fig. 4 we do not have the property that either $Q^{Tr}_{k,j} = 0$ or $Q^{Tr}_{k,-j} = 0$. This is because we have averaged over multiple spectra, each corresponding to one winter season. For some wavenumbers and levels, it is common to have either westward- or eastward-traveling waves depending on the winter, and so for the climatological spectra one can have traveling wave contributions in both directions at the same absolute frequency.

Figure 4 shows that standing waves explain the largest portion of the variance of $Z^{*\prime}$ at most wavenumbers and especially for low frequencies at the given latitude and pressure levels. An exception is for wave 1 and wave 2 at 500 hPa, and to a lesser extent 100 hPa, where there is a substantial westward-traveling peak in the spectrum at a period of approximately 25 days. This feature has been identified before by Speth and Madden (1983) and others. As well, in the midstratosphere there are eastward-traveling wave-2 and wave-3 components, although wave 3 explains a very small portion of the variance here. Finally, Fig. 4 also shows that the covariance term explains a significant portion of the total variance, typically being roughly similar to the variance explained by the traveling component.

d. *Frequency-integrated Northern Hemisphere spectra*

To better appreciate the contributions of standing and traveling waves throughout the atmosphere, we integrate the individual spectra (the total, standing, traveling, and covariance parts) over frequency to find the climatological variance explained by each of these portions for each wavenumber, at all latitudes and levels. The total and standing spectra are integrated over all frequencies, whereas the traveling and covariance parts

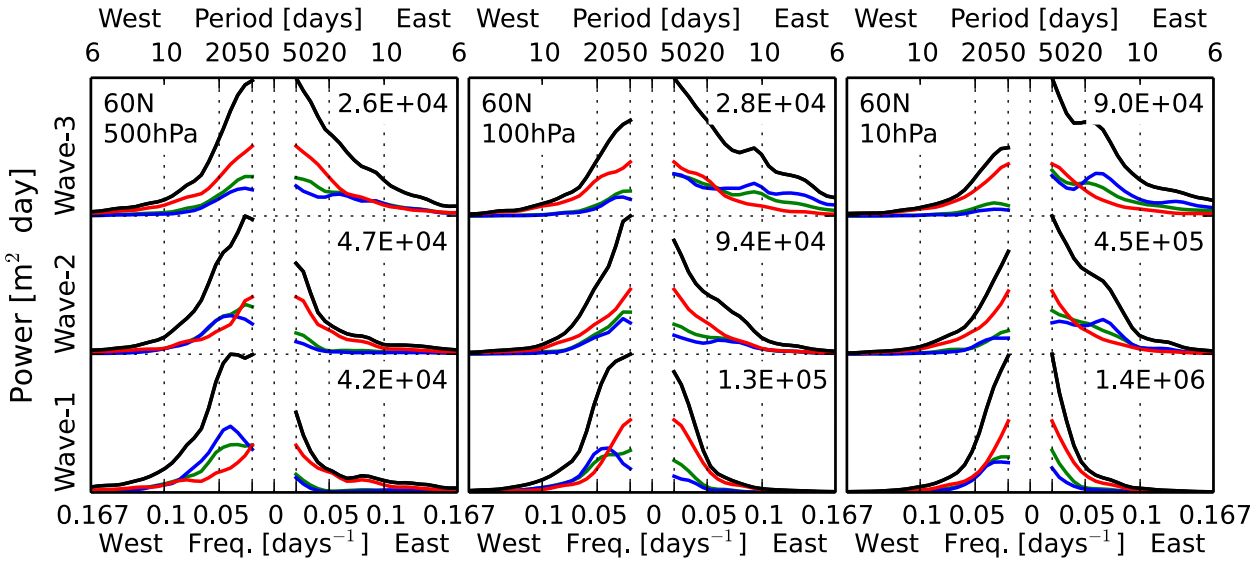

FIG. 4. The climatological wavenumber–frequency spectrum of $Z^{*\prime}$ for NDJFM at 60°N and (left) 500, (middle) 100, and (right) 10 hPa. Black is $(Z_{k,j})^2$, red is $(Z^{\mathrm{St}}_{k,j})^2$, blue is $(Z^{\mathrm{Tr}}_{k,j})^2$, and green is $2Z^{\mathrm{St}}_{k,j}Z^{\mathrm{Tr}}_{k,j}$. Only the first three wavenumbers and periods to 6 days are shown. Smoothing is as in Fig. 3c. All wavenumbers and levels are plotted using different scales, which are shown in the top-right corner of each plot, indicating the maximum value (m^2 day) reached by the total spectrum for that wavenumber and level. The spectra are normalized by $2/N^2T$ so that integrating over frequency and summing over wavenumber will recover the total variance of the original signal.

are integrated separately over negative and positive frequencies to isolate the eastward and westward components. These quantities are shown for the Northern Hemisphere in Fig. 5. We separately show the contributions by waves 1–4 and sum together the contributions from waves 5–10. Note the logarithmic scale for the contours: each contour represents a doubling of variance. Furthermore, in each row, the five right panels summed together give the leftmost panel.

The most important points to take from Fig. 5 are the following. As expected by the Charney–Drazin criteria, the stratospheric anomalies are dominated by wave 1 and wave 2 and, to a lesser extent, wave 3. In the stratosphere, the standing waves typically explain about half the total variance and the remaining variance is distributed roughly equally between the four remaining categories for wave 1, while for waves 2 and 3 there is more power in the eastward-traveling and covariance parts than in the westward parts. In the troposphere there is a largely different distribution of variance. In terms of wavenumber, the maximum contribution depends on the latitude: at very high latitudes (north of 75°) wave 1 makes the largest contribution, while moving to lower latitudes, larger wavenumbers tend to make relatively larger contributions. Furthermore, at very high latitudes standing waves explain a majority of the variance of wave 1, while between 60° and 80°N there is a substantial westward-traveling and covariance contribution. This was noted previously in Fig. 4. Moving to higher wavenumbers, there is generally a diminishing contribution from standing waves and an increase in the variance explained by eastward-propagating waves instead of westward-propagating waves, as we expect from the simple β-plane Rossby wave dispersion relation. For synoptic-scale disturbances (waves 5–10), the majority of the variance is explained by eastward-traveling waves in the midlatitudes, as expected.

The westward and eastward covariance portions, in the two right columns of Fig. 5, are generally similar in structure and amplitude to the respective westward- and eastward-traveling variances. We do not necessarily expect to find any independent information in the covariance plot: by the construction of the standing–traveling decomposition, the covariance between the two wave structures at some wavenumber and frequency is entirely determined by the amplitudes (or variances) of the individual standing and traveling parts [see Eq. (6)].

e. *Relative structure of standing and climatological wave*

Having established the importance of standing waves throughout the extratropical atmosphere, we now seek to understand their zonal structure. In particular, we wish to know whether the nodes and antinodes of these standing waves have preferred longitudinal positions. If so, and if the antinodes are in alignment with the maximum and minimum of the climatological wave, then the standing waves will primarily be driving amplification

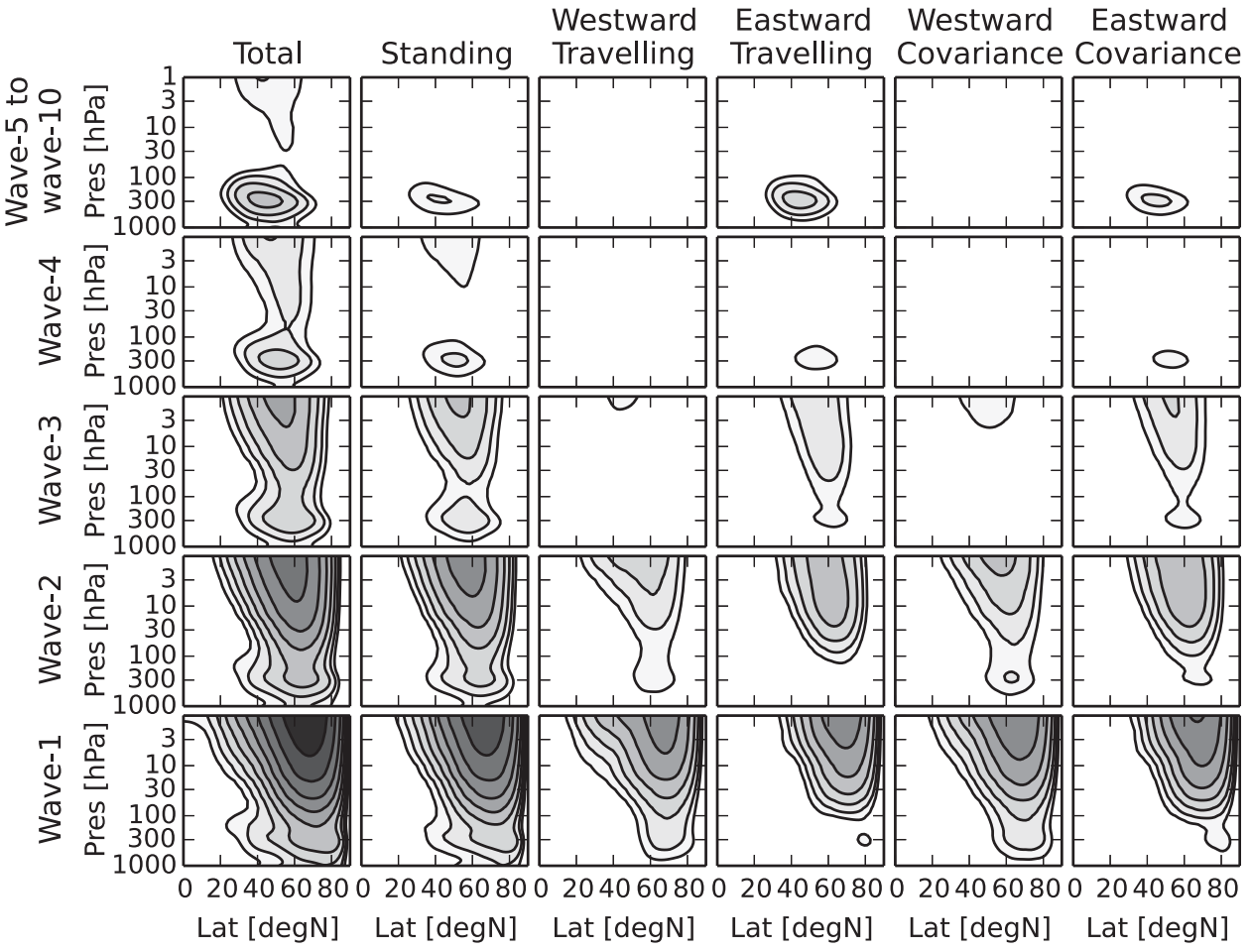

FIG. 5. The total variance integrated over frequency of various components of wavenumber–frequency spectra of $Z^{*\prime}$ for NDJFM in the Northern Hemisphere. (left)–(right) The total power spectrum (positive and negative frequencies), the standing variance (positive and negative frequencies), the traveling variance (westward) and the traveling variance (eastward), the standing–traveling covariance (westward), and the standing–traveling covariance (eastward). (bottom)–(top) Wave 1, wave 2, wave 3, wave 4, and sum from wave 5 to wave 10. The contour values are the same in all subplots: (8, 16, 32, 64, 128, 256, 512, 1024, 2048, 4096) $\times$ 10^2 m^2.

and attenuation of the climatological wave (instead of, for example, a zonal shift of the climatological wave). This would imply that the standing waves would be efficient drivers of the linear part of the vertical flux of Rossby wave activity, denoted LIN in section 1 (Smith and Kushner 2012).

Figure 6 shows the climatological time variance of $Z^{*\prime}_{\mathrm{St}}$ [see Eq. (10)] over November–March (NDJFM) for wave 1 and wave 2 at 500, 100, and 10 hPa, as well as the climatological wave-1 and wave-2 Z^{*}_{c} at these levels. The presence of zonal maxima of variance, especially in wave 1, indicates that the standing waves do have preferred spatial positions. This can be confirmed by plotting a histogram of the phase $\overline{\phi}_{k,j}$ [Eq. (8)] computed for all winter seasons and for all frequencies with significant power (not shown).

Focusing on wave 1, Fig. 6 shows that the relationship between the structure of the standing waves and the climatological wave changes substantially at different vertical levels. To clarify this point, we have plotted the longitude of the zonal maxima of the standing wave variance in the purple line and the longitude of the zonal extrema of the climatological wave in the green line. We can see that at 500 hPa, the maximum of the standing wave variance is at a much more northerly latitude than the maximum of the climatological wave and is zonally positioned near the zero lines of the climatological wave. On the other hand, at 100 hPa and to a lesser extent 10 hPa, the maximum of the standing wave variance is closely aligned with the climatological wave. This suggests that the wave-1 standing waves will be important drivers of linear interference effects at these levels. Note that although the wave-2 standing waves are weaker, they also have preferred zonal positions and are typically well aligned with the climatological wave 2,

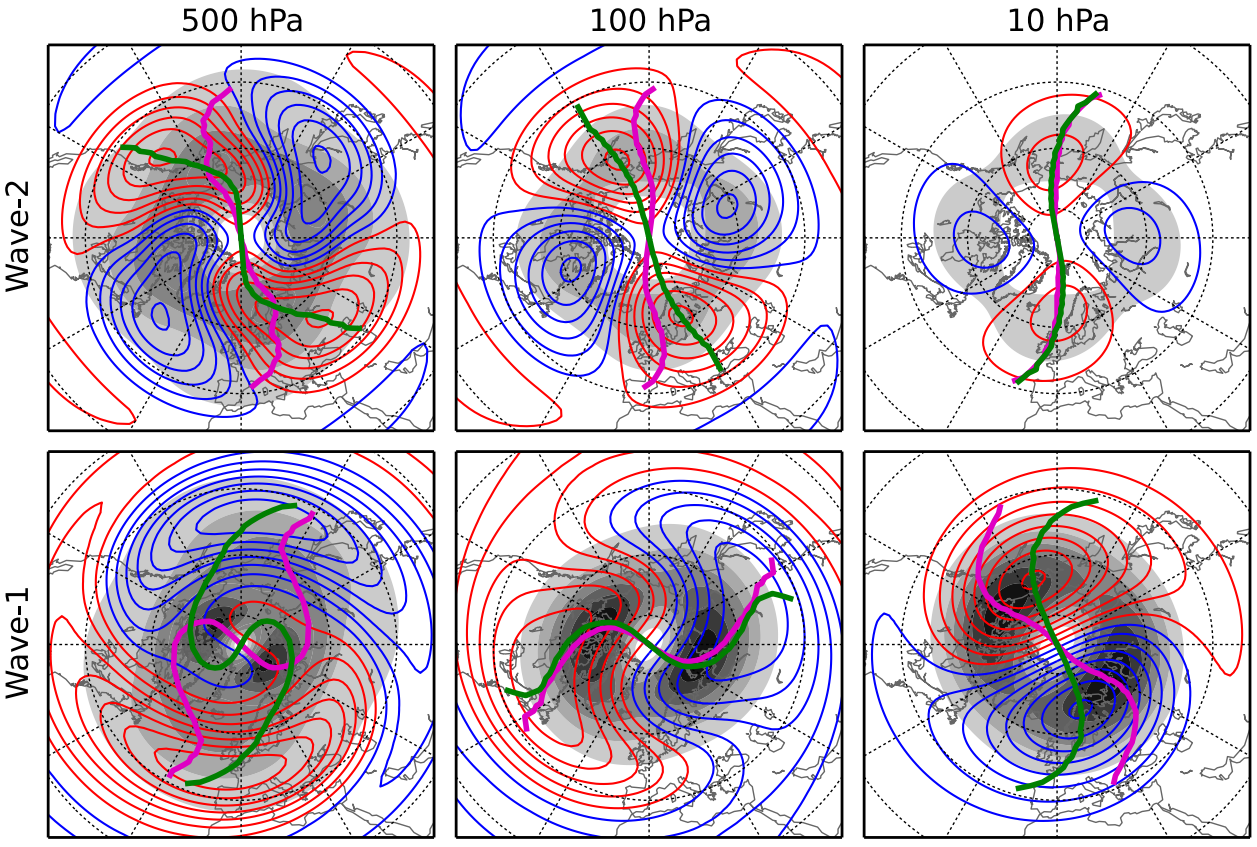

FIG. 6. Shading: variance over time of $Z^{*\prime}_{\mathrm{St}}$, as in Eq. (10), computed individually for each winter season, then averaged over all years. Contours: climatological wave Z^{*}_{c} averaged over NDJFM. (bottom) Wave 1 and (top) wave 2 at (left) 500, (middle) 100, and (right) 10 hPa. The shaded contours are, from (left) to (right), $(0, 6, \ldots, 48) \times 10^2$, $(0, 2, \ldots, 14) \times 10^3$, and $(0, 15, \ldots, 105) \times 10^3$ m^2. The colored line contours are, from (left) to (right), $\pm(7, 21, 35, \ldots, 119)$, $\pm(12, 36, 60, \ldots, 156)$, and $\pm(40, 120, 200, \ldots, 640)$ m. Blues are negative and reds are positive. The contours are the same for wave 1 and wave 2. The thick purple and green lines show the positions of the zonal extremes of, respectively, the variance over time of $Z^{*\prime}_{\mathrm{St}}$ and the climatological wave Z^{*}_{c}. These lines are only plotted north of 40°N.

implying they are also expected to efficiently contribute to linear interference effects.

f. Vertical wave structure and propagation

The spectra shown thus far are computed independently at each pressure and latitude and so do not convey a sense of the vertical or meridional structure of the waves. Thus, although Fig. 6 shows a general westward tilt with height of the crests and troughs of the standing wave-1, we have no guarantee that individual standing waves indeed span these vertical levels and have such a tilt. In this section we further explore these structures and their time dependence by employing the time-lagged wave amplitude and phase correlation statistics of Randel (1987); see also Shaw et al. (2010). This method computes the spatially remote time-lagged coherence and relative phase of a certain wavenumber.

The required information for the analysis is the time-dependent spatial Fourier amplitudes and phases of geopotential height, which we compute from our already-calculated 2D Fourier coefficients $\hat{z}_{k,j}$. See section 2 of Randel (1987) for details of the computation of the correlation coherence and phase. We separately calculate the correlations based on the total wave anomaly $\hat{z}_{k,j}$, the standing part $\hat{z}^{\mathrm{St}}_{k,j}$, the westward-traveling part ($\hat{z}^{\mathrm{Tr}}_{k,j}$, $j>0$), and the eastward-traveling part ($\hat{z}^{\mathrm{Tr}}_{k,j}$, $j<0$). However, we will omit the eastward-traveling wave coherence plot below because the eastward-traveling signal is very weak in the troposphere (see Fig. 4) and we are computing the correlations referenced to 500 hPa. We make the calculations for both wave 1 and wave 2. Equations (19) and (20), below, give the precise definitions of the standing and westward-traveling parts of the wave anomaly for a particular wavenumber k'.

Figure 7 shows a pressure-versus-lag cross section at 60°N of the wave-1 and wave-2 correlation coherence and phase with respect to 60°N and 500 hPa for the total wave anomaly (left column), the standing wave (middle column), and westward-traveling wave (right column).

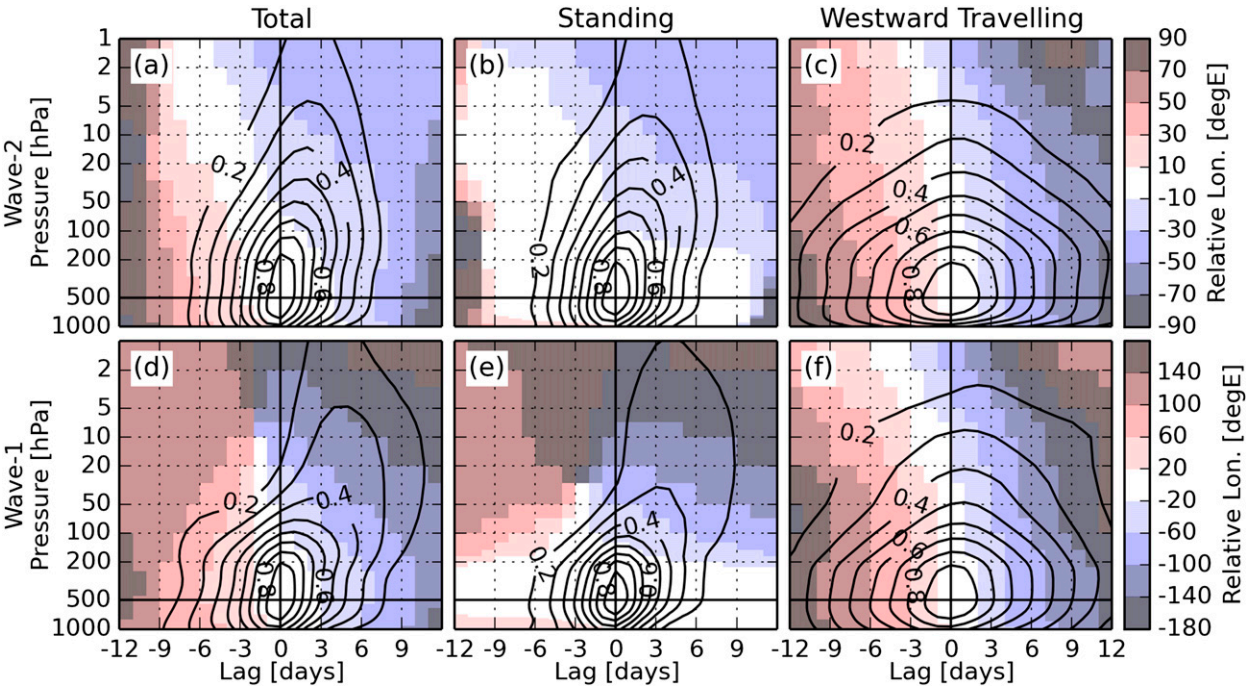

FIG. 7. Correlation coherence (contours) and phase (shading) of (a)–(c) wave-2 and (d)–(f) wave-1 geopotential height anomalies during NDJFM at 60°N as a function of pressure and lag with respect to 60°N and 500 hPa. Correlations are computed using (left) the total wave anomaly, (middle) only the standing part, and (right) only the westward-traveling part [see Eqs. (19) and (20)]. The coherence is plotted at intervals of 0.1, starting from 0.2. The phase (°) denotes the longitudinal separation of the two wave crests: positive phase means the distant (away from 0-day lag and 500 hPa) wave is eastward of the reference wave.

Shaw et al. (2010), using a shorter dataset and hence fewer degrees of freedom, estimate that coherences above 0.18 are statistically significant at the 99% level. We only plot coherences of 0.2 or above and are thus assured that the coherences shown are all significant at least at the 99% level. Focusing first on the total wave-1 anomalies (Fig. 7d), we see evidence for the well-known upward propagation of wave 1: for positive 3–6-day lags, there is a strong (>0.3) coherence between wave amplitudes at 10 hPa and the reference point at 500 hPa. Furthermore, at 0-day and positive lags, the wave 1 has a westward tilt with height throughout the upper troposphere and stratosphere—further evidence for the upward propagation of the wave. There is a suggestion of downward propagation for negative lags in the phase diagram (eastward phase tilt with height) but no such indication in the coherence diagram. This is partially due to using the entire NDJFM period to compute the correlations: as shown in Shaw et al. (2010), wave reflection has a strong seasonal cycle and peaks in strength in January–March (JFM). Furthermore, stronger couplings to the stratosphere, both upward and downward, are seen if a meridional average [e.g., from 45° to 80°N as in Shaw et al. (2010)] is performed before computing the correlations. We choose to perform the correlations based on 60°N for easy comparison with results we have already shown based solely on this latitude (e.g., in Figs. 1 and 4). Last, we note the clear tendency of westward propagation of wave 1 throughout the troposphere, as seen in the steadily decreasing phase with lag in Fig. 7d. Generally, the same conclusions can be reached for the total wave-2 signal (Fig. 7a) except that the time scale for upward propagation is faster (2–3 days) and there is no eastward phase tilt with height at negative lags.

Now we examine the correlations separately for the standing and westward-traveling parts of the wave-1 and wave-2 geopotential height anomalies, which are specifically given by (for some wavenumber k')

$$z^{\mathrm{St}}_{k'}(\lambda,t)=\frac{2}{NT}\sum_{j=-T_2}^{T_2}Z^{\mathrm{St}}_{k',j}\cos(k'\lambda+\omega_j t+\phi_{k',j}) \quad \text{and} \tag{19}$$

$$z^{\mathrm{TrW}}_{k'}(\lambda,t)=\frac{2}{NT}\sum_{j=1}^{T_2}Z^{\mathrm{Tr}}_{k',j}\cos(k'\lambda+\omega_j t+\phi_{k',j}). \tag{20}$$

Here, $Z^{\mathrm{St}}_{k',j}$ and $Z^{\mathrm{Tr}}_{k',j}$ are respectively the wave-k' standing and traveling amplitudes of the geopotential height

anomaly at frequency ω_j and $\phi_{k',j}$ is the wave-k' phase at frequency ω_j. Note that in Eq. (20) we sum over only positive j in order to isolate the westward-traveling waves.

Examining Fig. 7e, we see that for wave 1 the standing wave coherence is similar to the total wave coherence, but with generally smaller coherences throughout. The correlation phase for the standing wave is analogous to that for the total wave, but without the westward propagation in the troposphere. In addition, the westward and eastward phase tilts with height for positive and negative lags tend to be more extreme for the standing wave as compared to the total wave. As expected from the definition of the standing wave, at 500 hPa we see essentially no change in the phase of the wave with time for the lags shown, although at approximately ±14 days (not shown) there is a sharp 180° jump in phase, which would be in accordance with a standing wave with a 28-day period. For wave 2 (Fig. 7b), there is a very close correspondence between the coherence plots of the standing and wave and the total wave, and there is no change in phase until lags of ±10 days.

The westward-propagating wave-1 and wave-2 anomalies (Figs. 7c and 7f) are vertically deep signals, spanning the troposphere and up to the midstratosphere at 0-day lag, with an equivalent barotropic structure in the troposphere and weak westward phase tilts with height in the stratosphere. Furthermore, they have a much longer coherence time scale (0.2 coherence up to ±13 days at 500 hPa for wave 1) compared to the total wave in both in the troposphere and in the stratosphere. The correlation phases show the expected consistent phase propagation, with a 360° revolution at 500 hPa being made in about 28 days for wave 1, roughly in accordance with the westward-traveling wave-1 spectral peak seen in the left panel of Fig. 4. These results agree with the vertical structure of Northern Hemisphere high-latitude westward-propagating wave-1 features identified by previous authors—for example, Fig. 11 of Branstator (1987) or Fig. 7 of Madden and Speth (1989). The eastward-traveling signals (not shown) are strongly trapped in the troposphere and the progression of phase is not as consistent as for the westward-traveling wave.

Note that largely the same conclusions can be reached by picking a reference point in the stratosphere—for example, at 60°N and 10 hPa (not shown). The standing wave amplitudes here are preceded by anomalies in the troposphere about 3–6 days before for wave 1 (less for wave 2), and the westward-propagating waves fill the depth of the stratosphere and troposphere with a barotropic structure in the troposphere and a slight westward tilt with height in the stratosphere. The eastward waves referenced to the stratosphere do not penetrate into the troposphere.

4. Summary and discussion

In this study we have introduced a novel decomposition of longitude- and time-dependent signals into standing and traveling components. Unlike previous techniques, our method explicitly provides the covariance between the standing and traveling waves and permits reconstruction of the standing and traveling signals. We apply the decomposition to geopotential height anomalies in the Northern Hemisphere winter. Focusing on planetary waves 1–3, we find that at 60°N the standing wave explains the largest portion of the variance in wave anomalies, especially at low frequencies. There are exceptions for wave 1 and to a lesser extent wave 2, which have substantial westward-traveling anomalies in the troposphere with periods around 25 days. In the stratosphere standing waves generally dominate, except for a small peak in the eastward-traveling wave 2 with a period of about 16 days.

We have also shown that planetary wave-1 and wave-2 standing wave anomalies have preferred longitudinal positions and that their antinodes generally align with the maximum and minimum of the climatological wave, especially in the lower and midstratosphere. This implies that the standing waves should be an efficient driver of LIN (Smith and Kushner 2012), which is the vertical flux of Rossby wave activity that is linearly dependent on the climatological wave pattern. This point will be examined in more detail in a subsequent paper. Last, we examined the vertical and time-lagged structure of the standing and traveling wave-1 and wave-2 signals with respect to 60°N and 500 hPa. We found that the standing waves have a similar structure to the total wave with a tendency for upward propagation from the troposphere to the stratosphere with a time scale of 3–6 (2–3) days for wave 1 (wave 2). On the other hand, the westward-traveling wave 1 and wave 2 are deep signals spanning the troposphere and stratosphere with relatively little phase tilt.

The separation of wave anomalies into standing and traveling parts is helpful for distinguishing the wave events that originate in the troposphere and drive stratospheric variability. Although, as we have shown, the westward-propagating wave 1 is a strong feature in the high-latitude troposphere and lower stratosphere; because of its lack of phase tilt, we do not expect it to strongly contribute to the vertical flux of wave activity. On the other hand, we have isolated standing waves and shown that they have a tendency to strengthen and weaken the climatological wave. In addition, the phase tilts and time-lagged coherences of the standing wave contributions are suggestive of upward propagation, and one would expect them to be responsible for the upward

communication of wave activity anomalies from the troposphere to stratosphere. Future work will quantify the contributions of the standing and traveling waves to wave activity flux variability over a range of time scales.

Acknowledgments. The authors thank Dr. Karen L. Smith for discussions during O.W.'s visit to the Lamont–Doherty Earth Observatory in 2013. We are also grateful for helpful comments from three anonymous reviewers. The authors acknowledge funding from the Natural Sciences and Engineering Research Council of Canada, the Ontario Graduate Scholarship program, and the Centre for Global Change Science at the University of Toronto. P. J. K. wishes to acknowledge helpful feedback received during the Kavli Institute for Theoretical Physics "Wave-Flow Interaction" program in 2014. This research was supported in part by the National Science Foundation under Grant PHY11-25915.

APPENDIX

Spectral Identities and Derivations

a. *Inverse Fourier transform of real signal*

The inverse 2D discrete Fourier transform is conventionally written as

$$q(\lambda,t)=\frac{1}{NT}\sum_{k=1}^{N-1}\sum_{j=0}^{T-1}e^{ik\lambda+i\omega_j t}\hat{q}_{k,j}. \tag{A1}$$

Noting that $\hat{q}_{k,j}=\hat{q}_{N+k,T+j}$ and assuming for convenience that N and T are odd (which is not strictly necessary), one can rewrite Eq. (A1) as

$$q(\lambda,t)=\frac{1}{NT}\sum_{k=-N_2}^{N_2}\sum_{j=-T_2}^{T_2}e^{ik\lambda+i\omega_j t}\hat{q}_{k,j}, \tag{A2}$$

where $N_2=(N-1)/2$ and $T_2=(T-1)/2$. Furthermore, given that $q(\lambda, t)$ is a real-valued function, we have $\hat{q}_{-k,-j}=(\hat{q}_{k,j})^{\dagger}$, where the dagger represents the complex conjugate. Thus, we can keep only half the Fourier coefficients. Recalling that $q(\lambda, t)$ has zero zonal mean, we can rewrite Eq. (A2) as

$$q(\lambda,t)=\frac{1}{NT}\sum_{k=1}^{N_2}\sum_{j=-T_2}^{T_2}e^{ik\lambda+i\omega_j t}\hat{q}_{k,j}+\frac{1}{NT}\sum_{k=-N_2}^{-1}\sum_{j=-T_2}^{T_2}e^{ik\lambda+i\omega_j t}\hat{q}_{k,j}. \tag{A3}$$

Then, using that

$$\begin{aligned}\sum_{k=-N_2}^{-1}\sum_{j=-T_2}^{T_2}e^{ik\lambda+i\omega_j t}\hat{q}_{k,j}&=\sum_{k=1}^{N_2}\sum_{j=-T_2}^{T_2}e^{-ik\lambda+i\omega_j t}\hat{q}_{-k,j}\\&=\sum_{k=1}^{N_2}\sum_{j=-T_2}^{T_2}e^{-ik\lambda-i\omega_j t}\hat{q}_{-k,-j}\\&=\left(\sum_{k=1}^{N_2}\sum_{j=-T_2}^{T_2}e^{ik\lambda+i\omega_j t}\hat{q}_{k,j}\right)^{\dagger},\end{aligned} \tag{A4}$$

where the second equality holds because we are summing over a symmetric (about zero) range of integers j, we see

$$q(\lambda,t)=\frac{2}{NT}\sum_{k=1}^{N_2}\sum_{j=-T_2}^{T_2}\mathrm{Re}(e^{ik\lambda+i\omega_j t}\hat{q}_{k,j}). \tag{A5}$$

Rewriting the Fourier coefficients in terms of their amplitudes and complex phases, $\hat{q}_{k,j}=Q_{k,j}e^{i\phi_{k,j}}$, we have our reformulated inverse 2D discrete Fourier transform:

$$q(\lambda,t)=\frac{2}{NT}\sum_{k=1}^{N_2}\sum_{j=-T_2}^{T_2}Q_{k,j}\cos(k\lambda+\omega_j t+\phi_{k,j}). \tag{A6}$$

It is trivial to rewrite this in the form of Eq. (2) given that $q(\lambda, t)$ as zero time mean.

b. *Longitude of standing wave antinodes*

Hayashi (1973, 1977) and Pratt (1976) provide a formula for computing the longitudes of the antinodes of the standing part of a signal in terms of the power spectra and cross-spectra of $c_k(t)$ and $s_k(t)$ (note, in this section, that we follow the notation of Hayashi and Pratt, as outlined in section 2c). In particular, Hayashi (1973) defines[3]

$$\alpha=\tan^{-1}\left[\frac{2K_{\omega}(c_k,s_k)}{P_{\omega}(c_k)-P_{\omega}(s_k)}\right] \tag{A7}$$

and shows that the longitudes of the maximum time variance of the signal are given by

$$\lambda=\frac{m\pi+\alpha/2}{k}, \tag{A8}$$

where m is an integer. We showed in section 2a that the longitudes of the antinodes of the standing wave at wavenumber k and frequency ω_j are given by

[3] Note Eq. (3.3) in Hayashi (1973) is erroneously missing the $\tan^{-1}$. See, for example, Eq. (13) of Pratt (1976) or Eq. (4.3) of Hayashi (1977).

$\lambda = (1/k)(m\pi - \overline{\phi}_{k,j})$ with $\overline{\phi}_{k,j}$ defined in Eq. (8). Thus, to demonstrate the equivalence between our formula and Hayashi's, we must show that $\alpha = -2\overline{\phi}_{k,j}$.

We begin by rewriting Eq. (7) in the form of Eq. (13). Note for simplicity we take $Q^{\mathrm{St}}_{k,j} = 1$, although the derivation holds generally. Straightforward algebraic manipulations can be used to show that

$$q^{\mathrm{St}}_{k,\pm j}(\lambda, t) = c_k(t)\cos k\lambda + s_k(t)\sin k\lambda\,, \tag{A9}$$

where

$$c_k(t) = (\cos\phi_{k,j} + \cos\phi_{k,-j})\cos\omega_j t + (-\sin\phi_{k,j} + \sin\phi_{k,-j})\sin\omega_j t \tag{A10}$$

and

$$s_k(t) = (-\sin\phi_{k,j} - \sin\phi_{k,-j})\cos\omega_j t + (-\cos\phi_{k,j} + \cos\phi_{k,-j})\sin\omega_j t\,. \tag{A11}$$

We now compute the Fourier transforms of $c_k(t)$ and $s_k(t)$ in order to be able to compute their power spectra and cross-spectra. That is, we decompose $c_k(t)$ and $s_k(t)$ as

$$c_k(t) = \hat{c}_{k,j}e^{i\omega_j t} + \hat{c}_{k,-j}e^{-i\omega_j t} \quad \text{and} \tag{A12}$$

$$s_k(t) = \hat{s}_{k,j}e^{i\omega_j t} + \hat{s}_{k,-j}e^{-i\omega_j t}\,, \tag{A13}$$

where

$$\hat{c}_{k,j} = \frac{1}{2}(\cos\phi_{k,j} + \cos\phi_{k,-j} + i\sin\phi_{k,j} - i\sin\phi_{k,-j}), \tag{A14}$$

$$\hat{s}_{k,j} = \frac{1}{2}(-\sin\phi_{k,j} - \sin\phi_{k,-j} + i\cos\phi_{k,j} - i\cos\phi_{k,-j}), \tag{A15}$$

and $\hat{c}_{k,-j} = (\hat{c}_{k,j})^{\dagger}$ and $\hat{s}_{k,-j} = (\hat{s}_{k,j})^{\dagger}$. Using these formulas, one can show that

$$P_{\omega}(c_k) = |\hat{c}_{k,j}|^2 = \cos^2\left(\frac{\phi_{k,j} + \phi_{k,-j}}{2}\right), \tag{A16}$$

$$P_{\omega}(s_k) = |\hat{s}_{k,j}|^2 = \sin^2\left(\frac{\phi_{k,j} + \phi_{k,-j}}{2}\right), \quad \text{and} \tag{A17}$$

$$K_{\omega}(c_k, s_k) = \mathrm{Re}(\hat{c}_{k,j}\hat{s}_{k,j}) = -\frac{1}{2}\sin(\phi_{k,j} + \phi_{k,-j}). \tag{A18}$$

Thus, substituting the above into Eq. (A7) we have that

$$\begin{aligned}\alpha &= \tan^{-1}\left\{\frac{-\sin(\phi_{k,j} + \phi_{k,-j})}{\cos^2[(\phi_{k,j} + \phi_{k,-j})/2] - \sin^2[(\phi_{k,j} + \phi_{k,-j})/2]}\right\} \\ &= -\tan^{-1}\left[\frac{\sin(\phi_{k,j} + \phi_{k,-j})}{\cos(\phi_{k,j} + \phi_{k,-j})}\right] \\ &= -(\phi_{k,j} + \phi_{-k,j}) = -2\overline{\phi}_{k,j}\end{aligned} \tag{A19}$$

as required.

c. *Variance over time*

Here, we show how the variance over time of a single-wavenumber signal can be rewritten as a sum over the Fourier coefficients. We consider

$$q_k(\lambda, t) = \frac{2}{NT}\sum_{j=-T_2}^{T_2} Q_{k,j}\cos(k\lambda + \omega_j t + \phi_{k,j}). \tag{A20}$$

We compute the variance over time of the single-wavenumber signal (assuming the time mean is zero)—a quantity that depends on longitude:

$$\begin{aligned}\mathrm{var}(q_k)(\lambda) &= \frac{1}{T}\sum_{t=0}^{T-1}[q_k(\lambda, t)]^2 \\ &= \frac{4}{N^2T^3}\sum_{j=-T_2}^{T_2}\sum_{j'=-T_2}^{T_2} Q_{k,j}Q_{k,j'} \\ &\quad \times \sum_{t=0}^{T-1}\cos(k\lambda + \omega_j t + \phi_{k,j})\cos(k\lambda + \omega_{j'} t + \phi_{k,j'}),\end{aligned} \tag{A21}$$

where we have substituted in Eq. (A20) and then changed the order of summation. Using the orthogonality of the cosine basis functions, one can show

$$\begin{aligned}&\sum_{t=0}^{T-1}\cos(k\lambda + \omega_j t + \phi_{k,j})\cos(k\lambda + \omega_{j'} t + \phi_{k,j'}) \\ &\quad = \frac{T}{2}\delta_{j,j'} + \frac{T}{2}\cos(2k\lambda + 2\overline{\phi}_{k,j})\delta_{j,-j'} \\ &\quad = \frac{T}{2}\delta_{j,j'} + \frac{T}{2}[2\cos^2(k\lambda + \overline{\phi}_{k,j}) - 1]\delta_{j,-j'}.\end{aligned} \tag{A22}$$

Substituting Eq. (A22) into Eq. (A21) we have our final result for the variance over time of our signal represented as a sum over the Fourier coefficients:

$$\mathrm{var}(q_k)(\lambda) = \frac{2}{N^2T^2}\sum_{j=-T_2}^{T_2}[Q_{k,j}^2 + 2Q_{k,j}Q_{k,-j}\cos^2(k\lambda + \overline{\phi}_{k,j}) - Q_{k,j}Q_{k,-j}]. \quad \text{(A23)}$$

REFERENCES

Baldwin, M. P., and T. J. Dunkerton, 2001: Stratospheric harbingers of anomalous weather regimes. *Science,* **294,** 581–584, doi:10.1126/science.1063315.

Branstator, G., 1987: A striking example of the atmosphere's leading traveling pattern. *J. Atmos. Sci.,* **44,** 2310–2323, doi:10.1175/1520-0469(1987)044<2310:ASEOTA>2.0.CO;2.

Dee, D. P., and Coauthors, 2011: The ERA-Interim reanalysis: Configuration and performance of the data assimilation system. *Quart. J. Roy. Meteor. Soc.,* **137,** 553–597, doi:10.1002/qj.828.

Di Biagio, V., S. Calmanti, A. Dell'Aquila, and P. M. Ruti, 2014: Northern Hemisphere winter midlatitude atmospheric variability in CMIP5 models. *Geophys. Res. Lett.,* **41,** 1277–1282, doi:10.1002/2013GL058928.

Fraedrich, K., and H. Böttger, 1978: A wavenumber-frequency analysis of the 500 mb geopotential at 50°N. *J. Atmos. Sci.,* **35,** 745–750, doi:10.1175/1520-0469(1978)035<0745:AWFAOT>2.0.CO;2.

Garfinkel, C., D. Hartmann, and F. Sassi, 2010: Tropospheric precursors of anomalous Northern Hemisphere stratospheric polar vortices. *J. Climate,* **23,** 3282–3299, doi:10.1175/2010JCLI3010.1.

Haurwitz, B., 1940: The motion of atmospheric disturbances on a spherical earth. *J. Mar. Res.,* **3,** 254–267.

Hayashi, Y., 1971: A generalized method of resolving disturbances into progressive and retrogressive waves by space Fourier and time cross-spectral analyses. *J. Meteor. Soc. Japan,* **49,** 125–128.

——, 1973: A method of analyzing transient waves by space-time cross spectra. *J. Appl. Meteor.,* **12,** 404–408, doi:10.1175/1520-0450(1973)012<0404:AMOATW>2.0.CO;2.

——, 1977: On the coherence between progressive and retrogressive waves and a partition of space-time power spectra into standing and traveling parts. *J. Appl. Meteor.,* **16,** 368–373, doi:10.1175/1520-0450(1977)016<0368:OTCBPA>2.0.CO;2.

——, 1979: A generalized method of resolving transient disturbances into standing and traveling waves by space-time spectral analysis. *J. Atmos. Sci.,* **36,** 1017–1029.

Lucarini, V., S. Calmanti, A. Dell'Aquila, P. M. Ruti, and A. Speranza, 2007: Intercomparison of the northern hemisphere winter midlatitude atmospheric variability of the IPCC models. *Climate Dyn.,* **28,** 829–848, doi:10.1007/s00382-006-0213-x.

Madden, R. A., 1979: Observations of large-scale traveling Rossby waves. *Rev. Geophys. Space Phys.,* **17,** 1935–1949, doi:10.1029/RG017i008p01935.

——, and P. Speth, 1989: The average behavior of large-scale westward traveling disturbances evident in the Northern Hemisphere geopotential heights. *J. Atmos. Sci.,* **46,** 3225–3239, doi:10.1175/1520-0469(1989)046<3225:TABOLS>2.0.CO;2.

May, W., 1999: Space-time spectra of the atmospheric intraseasonal variability in the extratropics and their dependency on the El Niño/Southern Oscillation phenomenon: Model versus observation. *Climate Dyn.,* **15,** 369–387, doi:10.1007/s003820050288.

Nishii, K., H. Nakamura, and T. Miyasaka, 2009: Modulations in the planetary wave field induced by upward-propagating Rossby wave packets prior to stratospheric sudden warming events: A case study. *Quart. J. Roy. Meteor. Soc.,* **135,** 39–52, doi:10.1002/qj.359.

Pratt, R. W., 1976: The interpretation of space-time spectral quantities. *J. Atmos. Sci.,* **33,** 1060–1066, doi:10.1175/1520-0469(1976)033<1060:TIOSTS>2.0.CO;2.

Randel, W. J., 1987: A study of planetary waves in the southern winter troposphere and stratosphere. Part I: Wave structure and vertical propagation. *J. Atmos. Sci.,* **44,** 917–935, doi:10.1175/1520-0469(1987)044<0917:ASOPWI>2.0.CO;2.

——, and I. M. Held, 1991: Phase speed spectra of transient eddy fluxes and critical layer absorption. *J. Atmos. Sci.,* **48,** 688–697, doi:10.1175/1520-0469(1991)048<0688:PSSOTE>2.0.CO;2.

Shaw, T. A., J. Perlwitz, and N. Harnik, 2010: Downward wave coupling between the stratosphere and troposphere: The importance of meridional wave guiding and comparison with zonal-mean coupling. *J. Climate,* **23,** 6365–6381, doi:10.1175/2010JCLI3804.1.

Smith, K. L., and P. J. Kushner, 2012: Linear interference and the initiation of extratropical stratosphere-troposphere interactions. *J. Geophys. Res.,* **117,** D13107, doi:10.1029/2012JD017587.

Speth, P., and R. A. Madden, 1983: Space-time spectral analyses of Northern Hemisphere geopotential heights. *J. Atmos. Sci.,* **40,** 1086–1100, doi:10.1175/1520-0469(1983)040<1086:STSAON>2.0.CO;2.

Tsay, C.-Y., 1974: A note on the methods of analyzing traveling waves. *Tellus,* **26,** 412–415, doi:10.1111/j.2153-3490.1974.tb01619.x.

von Storch, H., and F. W. Zwiers, 1999: *Statistical Analysis in Climate Research.* Cambridge University Press, 494 pp.

Wheeler, M., and G. N. Kiladis, 1999: Convectively coupled equatorial waves: Analysis of clouds and temperatures in the wavenumber–frequency domain. *J. Atmos. Sci.,* **56,** 374–399, doi:10.1175/1520-0469(1999)056<0374:CCEWAO>2.0.CO;2.

Zhang, C., and H. H. Hendon, 1997: Propagating and standing components of the intraseasonal oscillation in tropical convection. *J. Atmos. Sci.,* **54,** 741–752, doi:10.1175/1520-0469(1997)054<0741:PASCOT>2.0.CO;2.